HADRON CANCER THERAPY COMPLEX EMPLOYING NON-SCALING FFAG ACCELERATOR AND FIXED FIELD GANTRY DESIGN

Eberhard Keil[*], Andrew Sessler[†] and Dejan Trbojevic[**]

[*] *CERN, CH1211 Geneva 23, Switzerland*
[†] *Lawrence Berkeley National Laboratory, Berkeley CA 29720, USA*
[**] *Brookhaven National Laboratory, Upton NY 11973, USA*

Keywords: Cyclotron, cancer hadron therapy, FFAG cyclotron
PACS: 29.20.Hm, 29.27.Eg, 41.75.Ak, 41.85.Lc, 87.56.By

INTRODUCTION

Cancer proton therapy exists today in many medical facilities and many more are being built and planned throughout the world. These facilities consist of isochronous cyclotrons, scaling FFAGs and synchrotrons. In this paper we consider non-scaling FFAGs. The advantages of non-scaling FFAGs with respect to synchrotrons are the fixed magnetic field and possibilities of higher repetition rates for spot scanning. With respect to cyclotrons the advantage is very much reduced magnet weight and ease of changing the final energy. Because of the possibility of changing energy and location with each spot (having a repetition rate of about 100 Hz) the cancerous tumor can be carefully scanned in three dimensions. The energy variation, and transverse location of a spot, allows that the ion energy deposition inside of the patient, because of the ŞBragg peakŤ, is precisely at the desired location. The non-scaling FFAG adjusts the final energy by adjusting the number of turns during acceleration. The very strong focusing provides not only smaller aperture but also better orbit control than in cyclotrons, thus leading to lower losses.

We have worked on the subject before [1, 2, 3, 4, 5]. This paper is an expansion of [5]. Both [5] and this paper go beyond our previous work in presenting a complete complex, thus including a new design of the accelerator and, also, design of the gantry as well as discussion of the transfers from one element to the other. We have changed the rf acceleration from a frequency-modulated low-frequency system to a system with high-frequency and fixed-frequency that jumps harmonic number during the acceleration process.

TABLE 1. Beam Parameters of H^+ and C^{6+} in rings 1, 2, 3. Identical particle parameters at n-Extr and (n+1)-Inj. Harmonic numbers are selected in the ratio of circumferences.

Particle	H^+				C^{6+}			
Ring	1-Inj	1-Extr	2-Inj	2-Extr	2-Inj	2-Extr	3-Inj	3-Extr
Kin. En./u(MeV)	7.951	30.97	30.97	250	7.8934	68.801	68.801	400
β	0.1294	0.2508	0.2508	0.6136	0.1294	0.3645	0.3645	0.7145
$B\rho$(Tm)	0.4083	0.8107	0.8107	2.432	0.8107	2.432	2.432	6.3472
$\delta p/p$	-0.3301	$+0.3301$	-0.5	$+0.5$	-0.5	$+0.5$	-0.4459	$+0.4459$
Harmonic no.	1155	596	745	305	1451	515	618	315

[1] e-mail Eberhard.Keil@t-online.de
[2] e-mail AMSessler@lbl.gov
[3] Supported by the U.S. Department of Energy under Contract No. DE-AC03-76SF0009
[4] e-mail Trbojevic@bnl.gov
[5] Supported by the U.S. Department of Energy under Contract No. DE-AC02-98CH10886

ACCELERATOR COMPLEX

The facility consists of three rings. The smallest Ring 1 is for protons. The largest Ring 3 is for C^{6+}ions. The middle Ring 2 is both for protons and C^{6+}ions. There, the magnetic rigidities $B\rho$ are equal. Thus changing particle species does not necessitate changing the magnet excitation. The maximum kinetic energies at extraction are 250 MeV for the protons and 400 MeV/u for the carbon ions, as required by the therapy. Momentum p and magnetic rigidity $B\rho$ change by factors 1.9855, 3, and 2.6095, respectively, in Ring 1, Ring 2, and Ring 3, as presented in Tab. 1. The momentum offsets $\delta p/p$ are defined with respect to the central energies in each ring: in the first ring the central kinetic energy is E_k=19.46 MeV for protons, in the second ring the central kinetic energy for protons is E_k=118.4 MeV while, when the same ring is used for carbon ions, is E_k=31.185 MeV/u, the central kinetic energy in the third ring, used only for carbon ions C^{6+}, is E_k=208.96 MeV/u. The Tab. 1 also shows the parameters, which can be calculated without reference to particular lattices. The parameters in the 1-Inj column of the Ring 1 in Tab. 1 are chosen such that the particle speed $c\beta$ of the protons at injection into Ring 1 and that of the C^{6+}ions at injection into Ring 2 are equal, thus permitting the acceleration of both species in the same system of RFQ and linear accelerator.

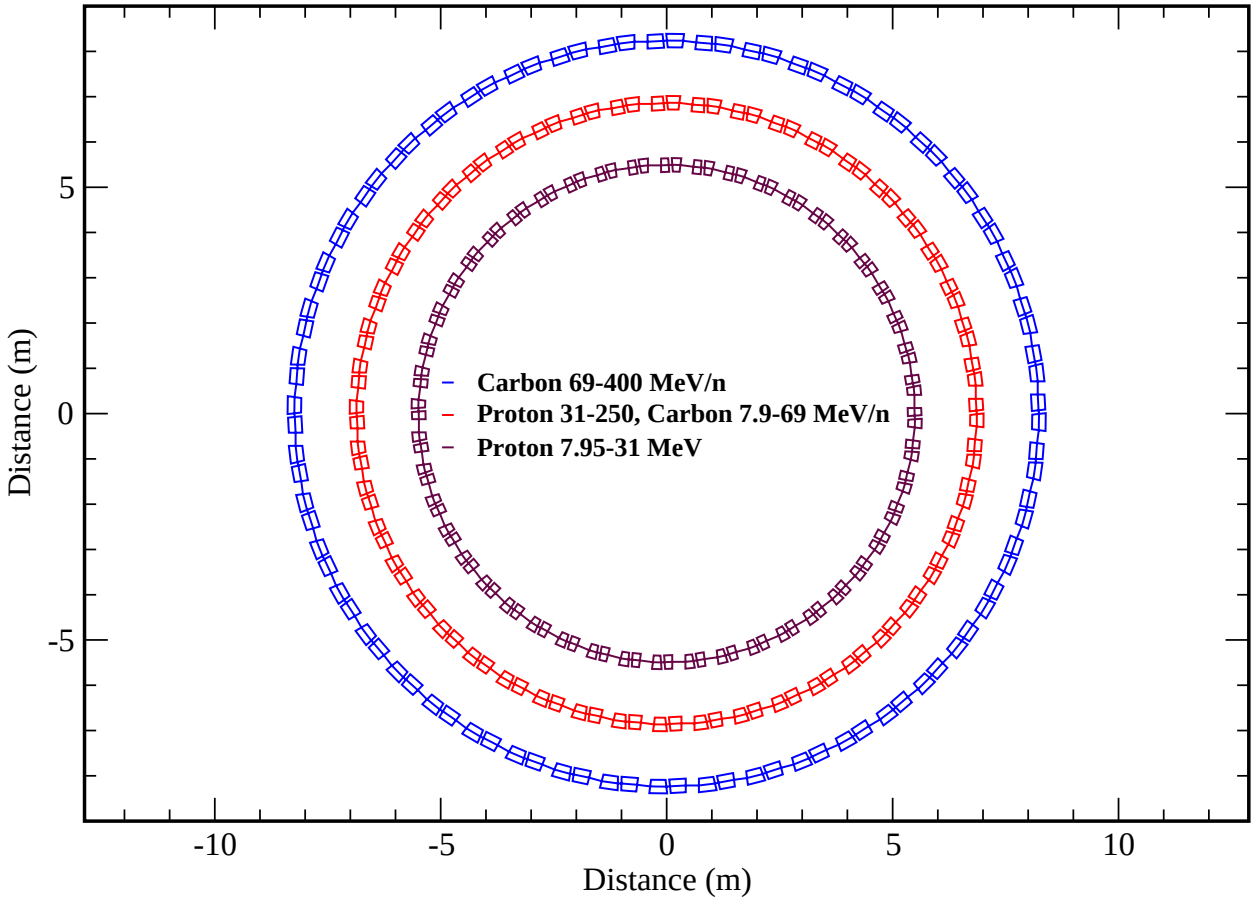

FIGURE 1. Schematic layout of the rings

Lattices

Tab. 2 shows the lattice and rf parameters in the proton and carbon machines. There is much similarity between them. All have 48 periods. The cell lengths are chosen in the ratio 4:5:6. As will be discussed in Section , we propose to accelerate at a constant rf frequency of about 1.3 GHz, employing harmonic number jumping during acceleration [6]. At the transfer from one ring to the other ring, the harmonic numbers are in the ratio of the circumferences, and transfer

of the bunches from the buckets in the first ring to buckets in the second ring is possible. Tab. 1 shows the ranges of harmonic numbers, ignoring the small variation of the path length with $\delta p/p$.

TABLE 2. Lattice and rf Parameters. All rings have 48 cells.

Ring	1	2	3
Particle	H^+	H^+ & C^{6+}	C^{6+}
Cell length(m)	0.72	0.9	1.08
Circumference(m)	34.56	43.20	51.84
F magnet length(m)	0.17	0.26	0.35
D magnet length(m)	0.18	0.27	0.36
rf frequency(GHz)	1.3	1.3	1.3

For the focusing in all lattices we have a choice between doublets and triplets of combined function magnets. An argument in favour of doublets is the smaller magnet count in the ratio 2:3. Arguments in favour of triplets are a smaller ratio of the reverse bending in the F magnets to the bending in the D magnet, and, hence, smaller dipole fields, and the symmetry points at the centre of the D magnet and at the centre of the straight section between the triplets, where α_x, α_y, and D_x' vanish. We adopt doublet lattices. The straight section space for the rf cavities, 0.29 m, and the gap between the magnets, 0.08 m, are the same in all lattices. Figs. 2, 3 and 4 show the schematic layout and the orbit functions in Ring 1, Ring 2, and Ring 3, respectively, at their respective reference momenta. The dispersion D_x is very small.

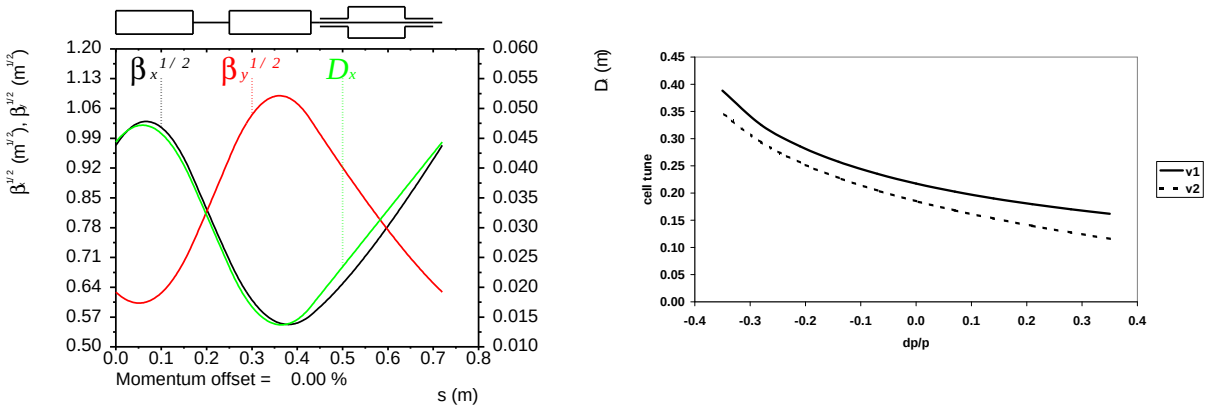

FIGURE 2. Schematic layout and orbit functions on the left, and horizontal phase advance μ_1 and vertical phase advance μ_2 on the right, in a cell of Ring 1 at the reference momentum $p_{\text{ref}} = 187.2$ MeV/c

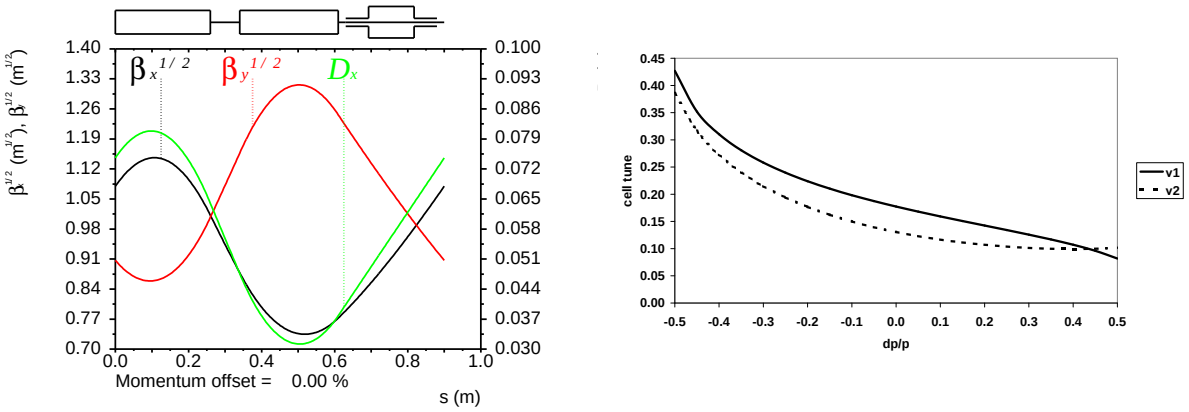

FIGURE 3. Schematic layout and orbit functions on the left, and horizontal phase advance μ_1 and vertical phase advance μ_2 on the right, in a cell of Ring 2 at the proton reference momentum $p_{\text{ref}} = 486.1$ MeV/c and at the C^{6+}ion reference momentum $p_{\text{ref}} = 2.917$ GeV/c

The phase advances at the reference energy are chosen such that both μ_1 and μ_2 stay below the systematic half integral resonance at $\mu_1 = \mu_2 = 0.5$ at the lower end and above $\mu_1 = \mu_2 = 0$ at the upper end of the energy range. Figs. 2, 3, 4 show the phase advance μ_1 and μ_2 in a cell of Ring 1, Ring 2, and Ring 3 as a function of the relative momentum deviation $\delta p/p$. The results in Figs. 2 to 9 were all calculated with the PTC_TWISS command in MAD-X [7]. In Fig. 2, μ_1 and μ_2 are well separated, and do not get too close to 0 and 0.5. In Fig. 3, μ_1 and μ_2 cross over, and μ_1 gets close to 0.5. The design involves rapid increase of the β-functions at the lower end of the $\delta p/p$ range, and the rapid increase of the radial offset at the upper end shown in Figs. shown in Figs. 5, 6 and 7, but the values are kept within tolerable ranges. A similar design principle had been adopted in FFAG rings for accelerating muons [8] and their electron model [9, 10, 11]. Since here both protons and carbon ions are non-relativistic, the variation of their time of flight with $\delta p/p$ is dominated by the variation of their speed $c\beta$, and the exact path length variation becomes irrelevant.

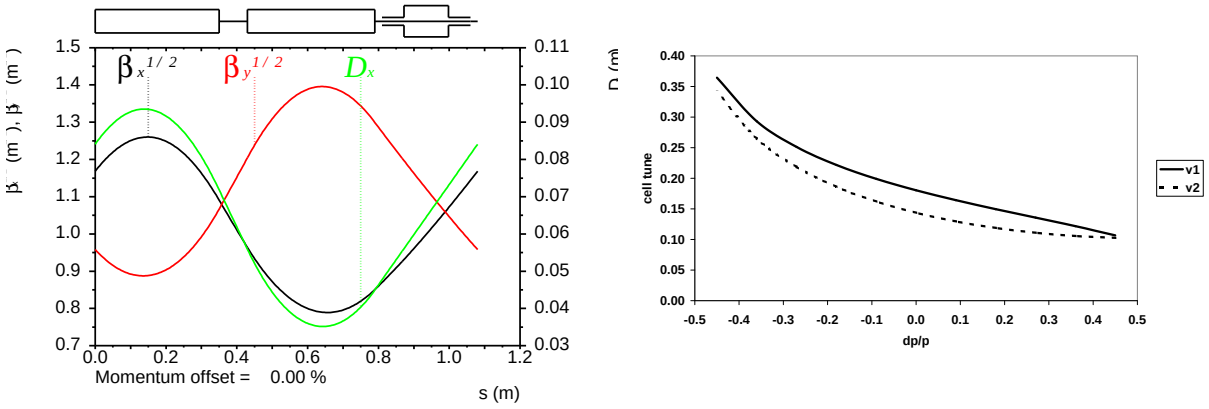

FIGURE 4. Schematic layout and orbit functions on the left, and horizontal phase advance μ_1 and vertical phase advance μ_2 on the right, in a cell of Ring 3 at the reference momentum $p_{\text{ref}} = 7.896$ GeV/c

Adjustable variables are the gradients and the shape of the dipoles. We have chosen the edge angles such that the end faces of the F magnets are parallel, while the angle between the end faces of the D magnets is twice the bending angle there. The fringe fields are treated in the hard edge approximation. Ring 2 is the most difficult one, since it has the largest ratio of extraction and injection momentum. Since we assume equal horizontal and vertical emittances throughout, coupling should have no consequences. In Fig. 3, μ_1 and μ_2 are not as well separated as in Fig. 2, and get closer to 0 and 0.5 than in Fig. 2.

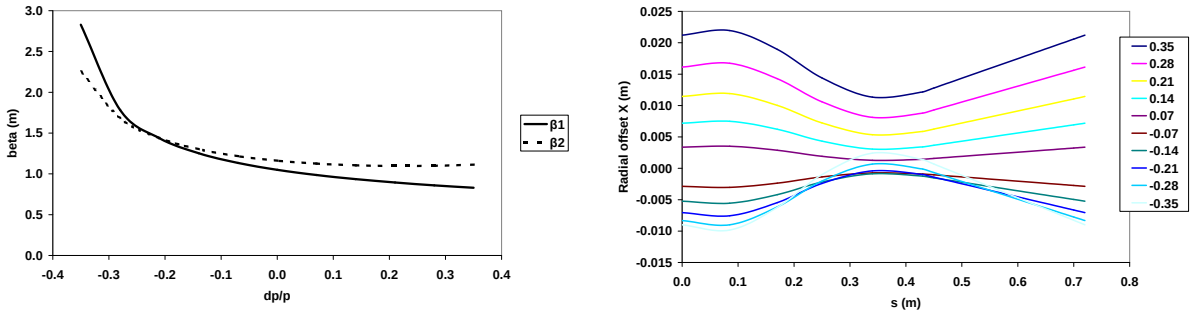

FIGURE 5. Maxima of horizontal β-function β_1 and vertical β-function β_2 to the left, and horizontal orbit offset X in m for a range of momentum deviation $-0.35 \leq \delta p/p \leq +0.35$ to the right in a cell of Ring 1

The bending angles in the cells are adjusted such that the path length variation at the reference energy with the relative momentum deviation $\delta p/p$ approximately vanishes to first order. The remaining path length variation is predominantly quadratic in $\delta p/p$. This is achieved by bending the beam away from the machine centre in the horizontally focusing F magnets. Figs. 5, 6, and 7 show the horizontal orbit offsets x along a cell of Ring 1, Ring 2 and Ring 3, respectively, for several values of $\delta p/p$ in the ranges of $\delta p/p$ required according to Tab. 1.

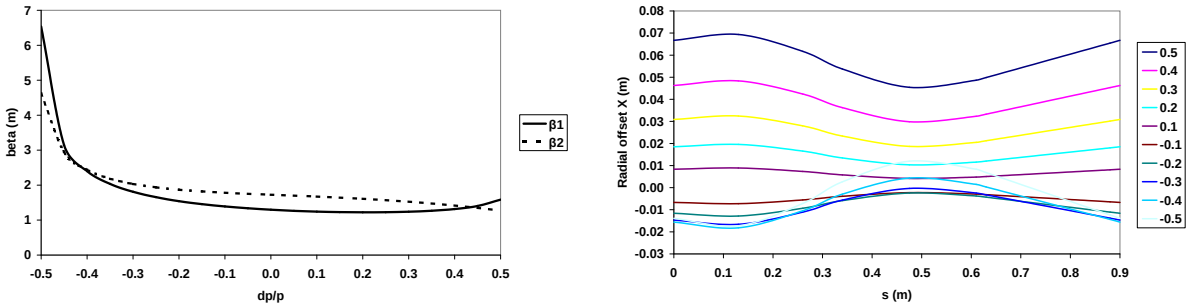

FIGURE 6. Maxima of horizontal β-function β_1 vertical β-function β_2 to the left, and horizontal orbit offset X in m for a range of momentum deviation $-0.5 \leq \delta p/p \leq +0.5$ to the right in a cell of Ring 2

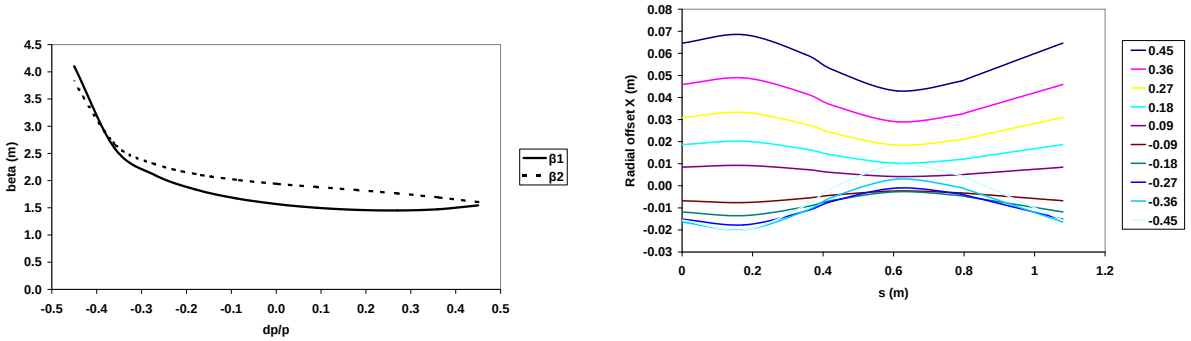

FIGURE 7. Maxima of horizontal β-function β_1 and vertical β-function β_2 to the left, and horizontal orbit offset X in m for a range of momentum deviation $-0.45 \leq \delta p/p \leq +0.45$ to the right in a cell of Ring 3

Aperture

For the calculation of the apertures, we assume a normalised emittance $\varepsilon_n = 0.5 \cdot 10^{-6}\pi$ m in both planes, following [12, 13], and allow for five rms beam radii in the half apertures. The vertical aperture radius A_y is determined by the amplitude of the vertical betatron oscillations. We use the ranges of $\delta p/p$ from Tab. 1, and take $|\delta p/p| \leq 0.35$ in Ring 1, $|\delta p/p| \leq 0.5$ in Ring 2, and $|\delta p/p| \leq 0.45$ in Ring 3. At all distances s along a cell, we look for the maximum value of β_y in those ranges, and obtain the vertical aperture A_y there. We calculate the contribution of the horizontal betatron oscillations to the horizontal aperture A_x in a similar manner. Because of the change of focusing with $\delta p/p$, the radial offset of the closed orbit is asymmetrical with respect to the reference orbit, as can be seen in Figs. 5, 6 and 7. Hence, we calculate and show the maximum positive and maximum negative horizontal orbit offsets x along a cell in the same ranges of $\delta p/p$. In the F magnets, where the offsets x are largest, the trajectories of the protons with increasing $\delta p/p$ are progressively more to the outside of the reference orbit. In the D magnets, where the offsets x are smallest, the trajectories of the particles with increasing $\delta p/p$ are not in the same order. The trajectory with the smallest $\delta p/p$ is more outside than trajectories with intermediate values of $\delta p/p$.

At all s, we subtract five times the horizontal rms betatron beam radius from the maximum negative offset x to find the minimum inner horizontal aperture radius A_x. Similarly, we add five times the horizontal rms betatron beam radius to the maximum positive offset x to find maximum positive horizontal aperture radius A_x. Figs. 8 and 9 show the maximum negative horizontal aperture radius and maximum positive horizontal aperture radius A_x and the vertical aperture radius A_y along s in Ring 1, Ring 2, and Ring 3. The latter has the largest aperture of the three rings, since the cells are the longest and the range of $\delta p/p$ is the largest.

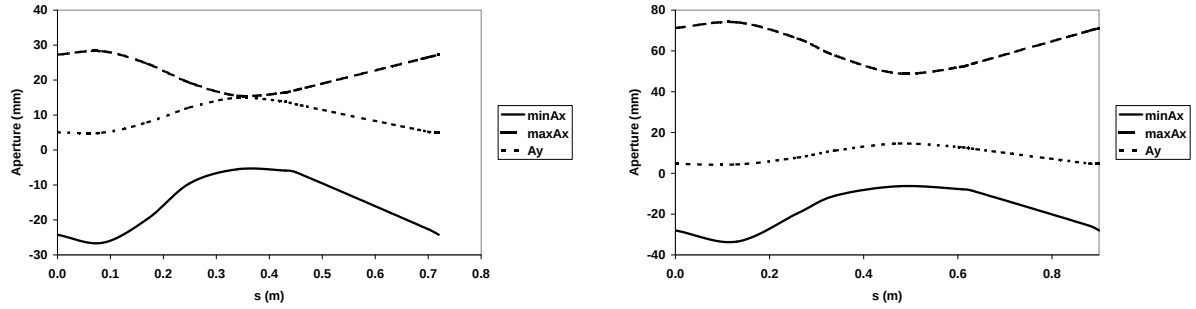

FIGURE 8. Inner and outer values of the horizontal aperture radius A_x and vertical aperture radius A_y in mm for a cell of Ring 1 for $-0.35 \leq \delta p/p \leq +0.35$ to the left, and for a cell of Ring 2 for $-0.5 \leq \delta p/p \leq +0.5$ to the right

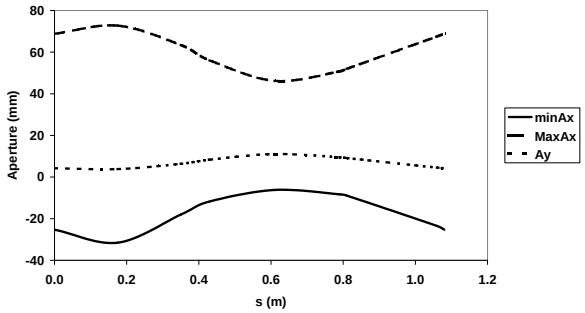

FIGURE 9. Inner and outer values of the horizontal aperture radius A_x and vertical aperture radius A_y in mm for a cell of Ring 3 for $-0.45 \leq \delta p/p \leq +0.45$

Acceleration

We adopt the scheme involving harmonic number h jumping [6]. The energy gain in a turn ΔE is adjusted such that the change in $c\beta$ causes a change of the revolution period by an integral number of rf cycles, and hence corresponds to an integral step Δh in h. Since $\Delta\beta/\beta = -\Delta h/h$, and $\mathrm{d}\beta/\mathrm{d}\gamma = 1/\beta\gamma^3$, it follows that $\Delta E = -E_0\beta^2\gamma^3\Delta h/h$, where E_0 is the rest energy of the particle. Hence, the smallest ΔE is achieved with $\Delta h = -1$ and large h. During acceleration, h decreases, since the revolution period decreases because of the increasing speed $c\beta$. At fixed Δh, ΔE increases rapidly during acceleration. Its variation can be reduced by starting acceleration with $|\Delta h| \gg 1$, gradually decreasing $|\Delta h|$, and switching to $\Delta h = -1$ towards the end [5].

The bunches are arranged in a train. The train occupies a fixed time interval ΔT, which is a small fraction of the revolution period at injection. This fraction of the revolution period grows during acceleration. The fraction of the circumference not occupied by the bunch train is useful for at least two purposes, for the rise time of kicker magnets, and for the rf manipulations outlined below.

As can be seen in the example that follows, the harmonic number scheme involves a significant change in the energy gain per turn during acceleration. This variation can be accomplished in several ways. One possibility is a rapid

TABLE 3. RF system parameters at $f_{\mathrm{RF}} \approx 1.3$ GHz, initial and final harmonic numbers h_i and h_f, initial step $|\Delta h|$, number of turns, maximum circumferential voltage V

Ring		h_i	h_f	$\lvert\Delta h\rvert$	turns	V(MV)
1	H^+	1155	596	8	293	0.11
2	H^+	745	305	25	116	2.4
2	C^{6+}	1451	515	27	253	0.61
3	C^{6+}	618	315	19	84	10.0

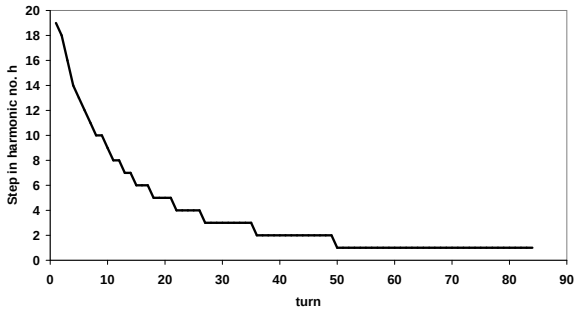

FIGURE 10. Variation of the harmonic number *h* in Ring 3

change of the rf cavity voltage (implying inefficient low *Q* rf cavities). Another possibility is a change of rf frequency during the passage of the gap between the bunch trains, such that the bunches arrive a different phase and experience a different acceleration per turn (implying a higher *Q* than the first scheme). A third possibility is programming voltage and frequency smoothly, such that the bunches arrive at the appropriate phases.

The harmonic number jumping scheme has an energy gain per turn that is much larger than that in a synchrotron. The high rate of acceleration ensures fast crossing of the resonances. Tab. 3 shows the main parameters of the rf systems that we arrived at, taking into account the considerations above. The number of turns is significantly smaller than the difference $(h_i - h_f)$, because of the initial step $|\Delta h| > 1$, and much smaller than it is in a synchrotron. Figs. 10 and 11 show how *h* and the circumferential accelerating voltage vary during acceleration in Ring 3 for C^{6+}. As shown in Fig. 11, there are about three large changes in the acceleration, the largest by almost a factor of two. In order to achieve this by changing the rf frequency, as discussed in the second scheme above, would be possible with a factor $Q < 1000$. Fig. 11 shows that the kinetic energy of the C^{6+} ions varies almost linearly.

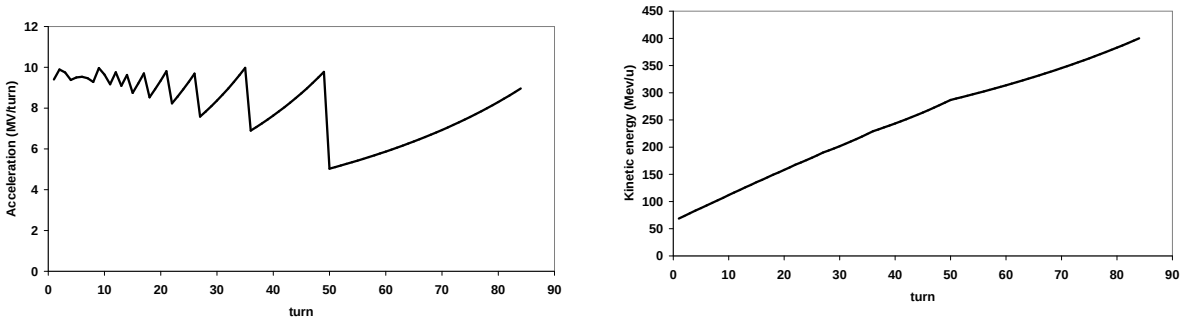

FIGURE 11. Variation of the circumferential accelerating voltage to the left, and variation of the kinetic energy per to the right, in Ring 3

Magnets

Tab. 4 shows the apertures and the fields of the combined function magnets. Their shape is discussed in Section . The inner and outer values of the horizontal aperture radius in the F and D magnets are calculated in the manner discussed in Section . The gradients *G* in the combined function dipoles cause a variation of the magnetic field across the horizontal aperture, quantified in the rows labelled field at min/max hor aperture. The fields in the F magnets change sign inside the horizontal aperture, those in the D magnets do not.

In Ring 1, the fields are below 1 T. The maximum field in Ring 2, 1.3 T, occurs in the D magnets at the inner horizontal aperture radius. The magnets in these rings are conventional iron-dominated magnets. They may be excited either by resistive room-temperature coils, or by coils made of high-temperature superconductor [14]. The maximum field in Ring 3 also occurs in the D magnets at the minimum horizontal aperture. At about 3.3 T, it is in the range of easy superconducting magnets. Suitable combined function magnets can be arrived at by scaling from the superconducting

TABLE 4. Magnet parameters, aperture in mm, fi eld B in T.

Magnet	F			D		
Ring	1	2	3	1	2	3
Inner hor apert radius	−27	−40	−32	−10	−13	−12
Outer hor apert radius	28	76	73	19	59	56
B at inner apert radius	−0.68	−1.40	−2.40	0.82	1.69	3.34
B at outer apert radius	0.17	0.57	0.81	0.44	0.50	1.30
Vert half apert	8	11	7	15	21	11

magnets in the proposed proton transport line for the J-PARC neutrino experiment [15] with $B = 2.59$ T, $G = 18.7$ T/m and a coil aperture radius $A = 86.7$ mm.

TABLE 5. Extraction kicker parameters

Ring	2	3
Kick angle/mrad	10.2	6.8
Rise time/ns	80	80
Aperture width/mm	107	94
Aperture height/mm	38	36
Kicker length/m	0.2	0.2
Kicker fi eld/T	0.13	0.22

Injection and Extraction

Extraction happens in two stages: (i) A full-aperture fast kicker magnet a long straight section deflects the extracted beam such that it is outside the circulating beam one or more cells downstream. The energy of the extracted proton beam can be varied in steps at most equal to the voltage V in Tab. 3 by accelerating for a variable number of turns, or half that value (in MeV/u) for the C^{6+} beam. We operate all rings with about 200 bunches, and leave about 1/3 of the circumference free for the extraction kicker rise time in Ring 3 and Ring 2 for H^+. There, the extraction kickers have the most demanding parameters. The required deflections may achieved more easily with a number of kicker magnets in neighbouring cells. The kicker parameters are shown in Tab. 5. The extraction kicker in Ring 1 and all injection kickers have longer rise times. (ii) A septum magnet deflects the extracted beam further, such that it misses components downstream, and sends it into a transfer line. Injection uses similar components in reverse order.

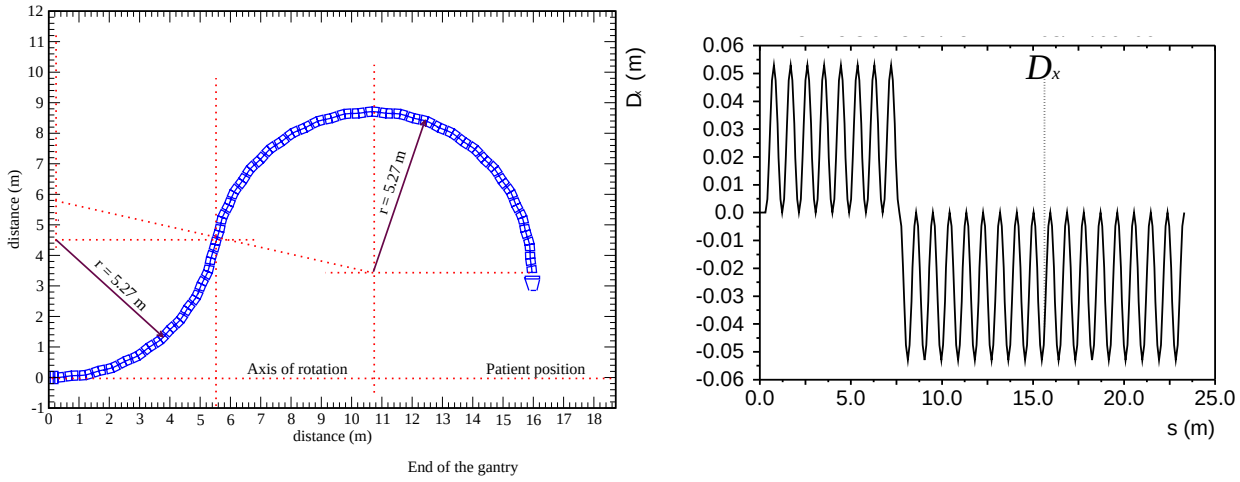

FIGURE 12. Schematic layout of the gantry to the left, and horizontal dispersion D_x in the gantry to the right

GANTRY

The beam is assumed to have equal emittances $\varepsilon_x = \varepsilon_y$. In the fixed transport line from the accelerators to the rotating gantry, it is matched to equal β-functions, $\alpha_x = \alpha_y = 0$, and $D_x = D'_x = 0$ at the junction. A 0.3-m-long straight matching insertion consists of two quadrupoles and two drift spaces, and rotates with the gantry, but remains on axis. It matches the round beam at the end of the transfer line to the gantry cells at any rotation angle. The gantry cells consist of non-scaling FFAG cells of combined function dipoles, arranged in the order FDDF. The bending angle of a cell is $\pm\pi/18$. The bending angles of the F and D magnets are adjusted such that $D_x = D'_x = 0$ at the centre of the D magnet. There, the curvature can be changed without harm to the matching of β-functions and dispersion D_x at $\Delta p/p = 0$. At the reference energy with $\delta p/p = 0$, the maximum β-functions are less than 1.63 m. The dispersion varies in the range $-55 \leq D_x \leq 55$ mm. Fig. 12 shows a schematic layout, and the matched dispersion. The first eight cells bend the beam away from the axis of rotation. The remaining seventeen cells have the opposite curvature, and bend the beam back towards the axis of rotation. The distance between the end of the gantry and the axis of rotation, as well as the maximum distance between the gantry and the axis of rotation, about 9 m in Fig. 12, can be varied by changing the number of cells. A similar gantry is in [16]. The gantry can transport particles with momentum deviation up to $\delta p/p = \pm 0.2$. With one excitation of the magnets it transports C^{6+}ions with kinetic energies between 195 and 400 MeV/u. With about 40% of that excitation it transports H^+ with kinetic energies between 118 and 250 MeV. A system of deflecting and focusing magnets at the end of the gantry compensates for lateral beam offsets (which are small), allows scanning, and achieves the desired beam size.

CONCLUSIONS

In this paper we have exhibited a design of a non-scaling FFAGs and a fixed-field gantry. We have designed a series of rings producing 200 MeV protons or 400 MeV/u carbon, designed an acceleration scheme, considered injection and extraction, developed a matched beam into the gantry, and presented a gantry design with compact magnets. The complex facility design is now ready for detailed engineering and costing.

REFERENCES

1. D. Trbojevic, A.G. Ruggiero, E. Keil, N. Neskovic, A. Sessler, Proc. Cyclotrons 2004, Tokyo, Japan (2004) 246. http://ribfweb1.riken.go.jp/cyc2004/proceedings/data/CYC2004_papers/19P31.pdf
2. E. Keil, A.M. Sessler, D. Trbojevic, Pres. at FFAG04 Workshop, Tsukuba, Japan, Oct 2004. http://hadron.kek.jp/FFAG/FFAG04_HP/pdf/keil.pdf
3. E. Keil, A.M. Sessler, D. Trbojevic, Proc. 2005 Particle Accelerator Conference, Knoxville, USA (2005) 1667.
4. D. Trbojevic, E. Keil, A. Sessler, Pres. at International Symposium on Utilisation of Accelerators, 5 to 9 June 2005, Dubrovnik, Croatia.
5. E. Keil, A.M. Sessler, D. Trbojevic, Proc. 2006 European Particle Accelerator Conference, Edinburgh (2006) 1681.
6. A.G. Ruggiero, BNL Doc. C-A/AP/237 (2006)
7. http://frs.home.cern.ch/frs/Xdoc/mad-X.html
8. E. Keil, A.M. Sessler, Nucl.Instr.Meth. A538 (2005) 159.
9. E. Keil, A.M. Sessler, CERN-AB-2003-095(ABP) (2003).
10. E. Keil, AB-Note-2004-011 (ABP) (2004).
11. E. Keil, J.S. Berg, A.M. Sessler, Proc. 2004 European Part. Accel. Conf., Lucerne, Switzerland, 587 (2004).
12. F. Gerigk (ed.) et al., CERN-2006-006 (2006).
13. S. Gammino, http://www.lns.infn.it/info/LNS_Activity,Report_2005/SEZ_E_Ion Sources and Accelerators/E_10.pdf
14. R. Gupta et al., Proc. 2005 Particle Accelerator Conference, Knoxville, USA (2005) 3016.
15. T. Nakamoto et al., Proc. 2005 Particle Accelerator Conference, Knoxville, USA (2005) 495.
16. D. Trbojevic et al., Proc. 2006 European Particle Accelerator Conference, Edinburgh (2006) 2352.